Journal of Materials Chemistry A

Evidence for Interfacial Geometric Interactions at Metal-Support Interfaces and Its Influence on the Electroactivity and Stability of Pt Nanoparticles

Journal:	*Journal of Materials Chemistry A*
Manuscript ID	TA-ART-11-2019-012456.R1
Article Type:	Paper
Date Submitted by the Author:	13-Dec-2019
Complete List of Authors:	Zhao, Xiao; Innovation Research Center for Fuel Cells, Gunji , Takao; University of Electro-Communications , Innovation Research Center for Fuel Cells Kaneko , Takuma ; University of Electro-Communications, Innovation Research Center for Fuel Cells Takao, Shinobu; University of Electro-Communications, Materials and Life Science Sakata, Tomohiro; The University of Electro-Communications Higashi, Kotaro; The University of Electro-Communications, Innovation Research Center for Fuel Cells Yoshida , Yusuke ; University of Electro-Communications, Innovation Research Center for Fuel Cells Ge, Junjie; Changchun institute of Applied chemistry, Liu, Changpeng; Changchun Institute of Applied Chemistry, State Key Laboratory of Electroanalytical Chemistry Xing, Wei; Changchun Institute of Applied Chemistry, Chinese Academy of Sciences, Zhu , Jianbing ; Department of Chemical Engineering, University of Waterloo Xiao, Meiling ; Department of Chemical Engineering, University of Waterloo Uruga, Tomoya; Japan Synchrotron Radiation Research Institute, Tao, Franklin; University of Kansas, Chen, Zhongwei; University of Waterloo, Chemical Engineering

Evidence for Interfacial Geometric Interactions at Metal-Support Interfaces and Its Influence on the Electroactivity and Stability of Pt Nanoparticles

Xiao Zhao,[a,f*] Takao Gunji,[a,f] Takuma Kaneko,[a,f] Shinobu Takao,[a] Tomohiro Sakata,[a] Kotaro Higashi,[a] Yusuke Yoshida,[a] Junjie Ge,[b] Changpeng Liu,[b] Wei Xing,[b*], Jianbing Zhu,[c] Meiling Xiao,[c] Tomoya Uruga,[e] Franklin (Feng) Tao[d] and Zhongwei Chen[c*]

[a] Innovation Research Center for Fuel Cells, The University of Electro-Communications, Chofugaoka, Chofu, Tokyo 182-8585, Japan

[b] State Key Laboratory of Electroanalytical Chemistry, Changchun Institute of Applied Chemistry, Chinese Academy of Sciences, Changchun, Jilin 130022, China

[c] Department of Chemical Engineering, University of Waterloo, Waterloo, Ontario, Canada

[d] Department of Chemical and Petroleum Engineering, University of Kansas, Lawrence, KS 66045, USA

[e] Japan Synchrotron Radiation Research Institute, SPring-8, Sayo, Hyogo 679-5198, Japan

[f] These authors contributed equally: X. Z., T. G., and T. K.

[*]e-mail: xiaozhao@uec.ac.jp, xingwei@ciac.ac.cn, and zhwchen@uwaterloo.ca

ABSTRACT: Supported metals are widely used as industrial catalysts wherein the supports affect catalytic performances remarkably through either electronic and/or geometric interactions with the metals, and/or providing interfacial synergistic sites. Herein, we observed evidence for interfacial geometric interactions (IGI) at Pt-C interfaces through a combination of atomic-scale structural analysis, in-situ X-ray absorption fine structure, and electrochemical measurements for Pt/C model systems. The IGI has a long-range attribute and affects Pt surface atoms not only at interfacial perimeters but also adjacent to interfaces. Those affected Pt surface atoms are proposed to contribute enhanced activity and stability for the oxygen reduction reaction through retarding the formation of strongly adsorbed oxygenated intermediates. Our work provides some necessary information for a better understanding of support effects and catalytically active surface sites.

INTRODUCTION

Supported metal atoms, clusters, and nanoparticles (NPs) are crucial materials in industrial catalysis.[1-11] For electrocatalysis, the metals, particularly Pt, supported on a spectrum of carbons are widely used for the oxygen reduction reaction (ORR), a key reaction to technologies of fuel cells and metal-air batteries.[1-3, 12-20] Both experiments and theoretical calculations reveal that the ORR overpotential on Pt originates from unfavorable -O and -OH binding energies that are about 0.2 eV and 0.1 eV stronger than the optimal values, respectively.[21-27] To weaken Pt-O/OH binding energies, the general routes are the modulation of chemical compositions, shapes, and core-shell structures of Pt-based NPs and thus the production of geometric and/or electronic/ligand effects.[14, 22] Supports are reported capable to affect selectivity and activity of supported metals through geometric and/or electronic interactions with metals,[28, 29] and/or interfacial synergistic effects.[8, 28, 30, 31] Assuming the understanding and the control of support effects were addressed well, the supports may provide an opportunity for further improving Pt-based electrocatalysts.

The supports not only stabilize the metal particles but also change their electronic structure and can tune their catalytic activity.[4, 6, 9, 28, 29, 32-39] The first-principles study of metal adatom adsorption on graphene showed that adatoms from groups I–III exhibit characteristics of ionic bonding and large interfacial charge transfer (ICT) and work-function shifts. Transition metal atoms with d valence electrons, noble metals, and group IV elements display covalent bonding characteristics with strong hybridization of adatom and graphene electronic states.[40] For example, the hybridization between the π orbitals of the polyaromatic hydrocarbons surface and the d orbitals of the Pt adatoms enhances the back-donation of electrons to the 2π* orbitals of the CO molecule.[29] Further, the electron transfer may depend on the adsorption configuration of metals. Mahmoodinia et al. showed, through the DTF, that in a complex of Pt_n- polyaromatic hydrocarbon, the atomic charge is positive on the Pt atoms and the dimers with a parallel configuration, while a negative charge is found on the upper Pt atom of Pt dimer with a upright configuration.[29, 33] On the other hand, in practical nanocatalysts, the discrepancy exists in literature with respect to the details of ICT even for the same system.[6, 35, 36] For instance, in Pt-NbO_x or Pt-NbO_x/C system,[6, 35, 36] the ICT directions from Pt to O or from O to Pt,[6, 35, 36] negligible ICT[37] and potential-dependent ICT[6] were reported. Moreover, the charge screening effect from the metal NPs is argued to limit ICT at a sub-nm range.[28, 41]

On the other hand, the lattice strains can modulate metal d states and thus their binding energies to reactive intermediates, which consequently changes the reactivity of the metals. The study of effect of

strain on the reactivity of metal surfaces was pioneered by Mavrikakis et al. by the DFT.[42] The geometrical strain effect operates by shifting the local d-band of the involved metals up or down and thus tuning reactivity of metals. For metals with more than half-filled d bands, the shortened interatomic distances (e.g. the geometrically compressive strain) increase the overlap of d-states and thus broaden d-band; meanwhile to keep d-band filling constant, the d-band shifts downward.[42-44] The metals with a downshifted d-band interact with the adsorbates in a weaker way and show a reduced reactivity. Compared with ICT, the lattice strains can influence metal atoms in a larger range,[27, 41, 45] which is intriguing as the interfacial strains is theoretically demonstrated[46, 47] and/or experimentally observed[48-52] due to the interfacial mismatch at metal-support interfaces. Gao et al. observed significant strain inside Au NPs near the stepped surfaces of rutile.[51] The interfacial compressive strain was also seen in $CoFe_2O_4$ NPs supported on graphene oxide sheets.[50] However, the fine understanding of interfacial geometric interactions (IGI, or, interfacial strains) and particularly their influence on properties of the metals remains difficult due to these reasons. (a) The metal-support interfaces are buried underneath metal NPs and thus hard to observe directly. (b) Both metal NPs and supports are structural heterogeneity in practical nanocatalysts. (c) The metal surfaces likely restructure in a reactive environment or during catalysis adopting geometric and electronic structures distinctly from their ex-situ state. (d) The ICT and IGI are often interrelated in a catalyst and hard to distinguish their single contribution to catalysis. To this end, Resasco et al recently highlighted the catalyst characterization via a combination of site-specific atomic-level measurement, for example, in-situ transmission electron microscopy (TEM) and sample-averaged techniques, for example, infrared spectroscopy is effective for the elucidation of structure−property relationships of supported catalysts.[53] Due to heterogeneous surface sites on the metals, the additional complex issue is where the catalytically active sites locate. The surface atoms at interfacial perimeters have been frequently suggested as active sites for catalysis.[8, 46, 54] Given the long-range attribute of IGI, the activated surface sites by IGI may be beyond interfacial perimeters.

In this work, we observed evidence for IGI by side-by-side comparing Pt/C model systems whose interfacial properties were controlled by the types of carbon support and the shapes and sizes of Pt NPs using a combination of atomic-scale structural analysis, in-situ X-ray absorption fine structure (XAFS) and electrochemical measurements. The IGI benefits both activity and stability of Pt NPs for the ORR, representing a desired structural effect for practical electrocatalysts. The Pt surface atoms not only at interfacial perimeters but also adjacent to interfaces are suggested with enhanced ORR activity by the IGI effect.

RESULTS AND DISCUSSIONS

Atomic-Scale Evidence for the IGI

We hypothesized IGI having a "long-range" attribute and impacting surface atoms more than a few atomic layers far from stressed metal-support interfaces, as seen in core-shell structured NPs[27] and heterogeneous thin films systems.[45] Thus, it is possible to directly observe the influence of IGI, for example, the changed interplanar spacings, on metal NPs that have the thickness of only several atomic layers. To this end, the ultrafine Pt NPs were controllably prepared and supported on two distinct carbon materials— carbon microcoils (CMC, see Fig. S1, ESI†) and Ketjen Black (KB) — to produce different Pt-C interfacial properties. The controllable synthesis of size- and shape-uniform Pt NPs was conducted by a pH-tuned ethylene glycol reduction method (see experimental details). The use of Pt/C is to avoid the alloying influences that can induce geometric and/or electronic effects. However, several structural factors still affect lattice strains of Pt NPs, for example, their sizes[55] and shapes.[56] Meanwhile, carbon surfaces are structural complex resulting from their intrinsic structural defects, surface doping, chemically functional groups, surface curvature and so on, which is, unfortunately, hard to control at a statistical level. With careful considerations of structural heterogeneities from both Pt NPs and carbon surfaces, we thus analyze lattice strains at the single-particle level in order to reduce structural variables as much as possible. We imaged individual Pt NPs and carbon surfaces using an aberration-corrected transmission electron microscopy (ATEM). Meanwhile, the in-situ XAFS and electrochemical measurements provide statistical-level structures-properties information.

Fig. 1

Fig. 1 shows those ultrafine Pt NPs, uniformly distributed on carbon surfaces (Fig. 1a-b), have an average size of about 2.1 nm (the insets in Fig. 1a-b) and adopt a shape of the cuboctahedron (Fig. 1c-d). As the free surfaces without the constraint from the supports contract inward and appear coordination-dependent,[57] here to separate origins of contraction from free surface and support influence, we strictly compared the two particles that have the same size, shape/facet distribution, and composition. As such, the coordination numbers-dependent surface contraction will be same between the two Pt NPs; and their difference in lattice strains could be safely ascribed to different interfacial properties. The two Pt NPs—the KB-Particle-1 from 2.1 nm Pt/KB and the CMC-Particle-1 from 2.1 Pt/CMC (Fig. 1c and Fig. 1d, respectively)—were selected because of their identical sizes and shapes. The averaged d{111} spacing for the CMC-Particle-1 (Fig. 1f) is 2.21 Å, which appears compressive

relative to the value of 2.29 Å for the KB-Particle-1 (Fig. 1e). On the {002} orientation, a phenomenon-similar but extent-different contraction was observed (Fig. S2). The anisotropic contraction at different orientations may originate from an anisotropic combination at Pt-CMC interfaces. As discussed above, the observed differences in interplanar spacings between the two Pt NPs stem from distinct Pt-C interfacial properties and indicate the "long-range" attribute of IGI.[27]

Fig. 2

The supplementary evidence arises from observing two Pt NPs that are both from 2.1 nm Pt/CMC and have similar sizes but different interfacial areas, that is, the CMC-particle-2 at the edge of CMC (Fig. 2a, b, c, g, h) and the CMC-particle-3 completely supported by CMC (Fig. 2d, e, f). Interestingly, the CMC-particle-3 with larger contact areas with CMC displays smaller interplanar spacings (d{111}= 2.17 Å), as compared with the CMC-particle-2 (d{111}= 2.26 Å). The fine examination of the CMC-particle-2 is shown in Fig. 2a and Fig. S3. A much smaller d{111} on the supported Pt region (2.18 Å) than on the unsupported domain (2.37 Å) was observed in the CMC-particle-2. This is a direct evidence for the existence of IGI because (i) supported and unsupported regions are in the identical nanoparticle with a small-enough size, about 2.3 nm; (ii) if there are any unknown factors, besides the IGI, affecting d{111} spacing, these factors should have equivalent effects on supported and unsupported regions; (iii) the only sharp difference is with and without Pt-CMC interfaces between them. Additionally, in the CMC-Particle-2, we observed the local dislocations that initiate at the nanoscale border and develop toward the outer of unsupported Pt domains presumably due to the uneven distribution of IGI. The dislocation is a kind of line defects and could induce local surface strain in lattices relative to the normal atomic arrangement. In this regard, the dislocation should affect the reactivity of NPs and deserve to study further. In a commercial Pt/C (TEC10E50E-HT, TKK), the Pt particle at the edges of carbon displays a similar phenomenon observed in the CMC-Particle-2 (Fig. S4), thereby suggesting an extension of IGI to other carbon-supported metals systems. Notably, only statistically-limited information obtained from the atomic-scale structural analysis is an inherent characteristic of high-resolution TEM technique. Here, to make individual NPs more representative for overall NPs, the main efforts were made in terms of controllable synthesis of shape- and size-uniform Pt NPs. Additional analysis of other Pt NPs from 2.1 nm Pt/CMC is shown in Fig. S5.

In-Situ Spectroscopic Evidence for the IGI

Fig. 3

To explore the influence of IGI on ORR performances of Pt NPs, we utilized in-situ XAFS, a sample-averaging technique, to characterize Pt NPs under reaction environment.[58-60] In-situ Pt L_3-edge X-ray absorption near edge structure (XANES) was collected as a function of applied potentials versus reversible hydrogen electrode (RHE). The in-situ XANES data reveals that the normalized white-line peak intensities (μ_{norm}) of Pt L_3-edge for both 2.1 nm Pt/CMC (Fig. 3a) and 2.1 nm Pt/KB (Fig. S6) increase with applied potentials due to the chemisorption of oxygenated species on Pt surfaces.[58, 61-64] However, the strong oxygen adsorption was suppressed on 2.1 nm Pt/CMC at 1.0 V (Fig. 3b) compared to 2.1 nm Pt/KB. Further, we analyzed the potential-dependent Δμ-XANES for Pt-L_3 edge, which can reveal changes in surface chemisorption of oxygenated species when changing potentials and represent a surface-sensitive technique.[21, 65, 44-47] The Pt L_3-edge Δμ-XANES was obtained relative to the μ_{norm} at 0.4 V, a potential at double layers with relatively free of surface adsorbates. As shown in Fig. 3c, the Δμ-XANES differs between the two catalysts. Specifically, when raising potentials from 0.4 to 0.8 V, the Δμ amplitudes are similar for the two catalysts; however, when elevating potentials from 0.8 to 1.0 V, a remarkably smaller Δμ amplitudes was observed on 2.1 nm Pt/CMC than on 2.1 nm Pt/KB, suggesting an inhibited adsorption of strongly-bonded oxygenated species on 2.1 nm Pt/CMC. As it has been well documented that the compressive strains on Pt can shift d-band center down and weaken binding strength to oxygenated species,[25, 27, 42] the in-situ XANES difference between the two catalysts is, thus, consistent with the observed compressive strains in 2.1 nm Pt/CMC as shown in the analysis of atomic-scale lattice strains. Extended X-ray absorption fine structure (EXAFS) spectra provide the local environment around the target atoms. The Fourier transformed EXAFS (FT-EXAFS) at 0.4 V in Fig. 3d shows that both 2.1 nm Pt/KB and 2.1 nm Pt/CMC did not present any scattering peaks that could be assigned to Pt-C or Pt-O shells except Pt-Pt peaks, suggesting the possible ICT is too weak or too few (if any) to be visible in EXAFS.

The absence of strong ICT in 2.1 nm Pt/KB and 2.1 nm Pt/CMC helps the exploration of IGI effect as the strong geometric and electronic interactions are often interrelated and coexist in other systems.[4, 6, 9, 35-39] On the other hand, the fitted structures at 0.4 V (other results are in Table S1, ESI†, Fig. S7 and Fig. S8) reveal a shortened Pt-Pt bond distance of 2.741±0.004 Å in 2.1 nm Pt/CMC compared to 2.749±0.012 Å in 2.1 nm Pt/KB, in line with the atomic-scale analysis of lattice strains. The relatively small difference in Pt-Pt bond length between the two catalysts may be due to that the EXAFS is a sample-averaging technique and detects all atoms in a catalyst. Moreover, the extent of lattice strains or particle deformation depends strongly on the strength of metal-support interactions. Thus, an additional factor for only a small decrease in Pt-Pt bond length may be the moderate metal-C interactions in 2.1

nm Pt/CMC compared to other strong metal-metal oxides interactions. For instance, a clearly decreased Pt–Pt bond distance and a strong ICT have been detected by the EXAFS in Pt/NbO_x/C system.[6] However, the weak or negligible ICT while the decent lattice strains in 2.1 nm Pt/CMC provide an opportunity to study IGI influences on electrocatalytic performances of Pt NPs.

Influence of the IGI on electrocatalytic performances of Pt NPs

Fig. 4

Enhanced ORR activity by the IGI: The ORR was used as a model reaction to scrutinize the influence of IGI on the electroactivity of Pt NPs. In Fig. 4a, the ORR polarization curves for 2.1 nm Pt/CMC show an anodic shift demonstrating its improved activity as compared with 2.1 nm Pt/KB. The calculated specific activity (SA, normalized by the electrochemical surface areas of Pt) and mass activity (MA, normalized by the mass of Pt) are about 2.1- and 2.0-times higher on 2.1 nm Pt/CMC than on 2.1 nm Pt/KB, respectively. A similar trend in ORR activity was observed between 2.1 nm Pt/CMC and a commercial 2.0 nm Pt/C (TEC10E20E, Fig. S9). On a combination of lattice strain analysis, in-situ XAFS data, and previous studies,[21-27] the improved SA on 2.1 nm Pt/CMC is ascribed mainly to IGI-induced compressive strains that shift d-state of Pt surface atoms down and thus weaken their binding energies to ORR intermediates.

Size-Dependent IGI effect: We explored a size-dependent IGI effect as the sizes of metal NPs affect overall interfacial areas and the fraction of surface atoms activated by IGI. As such, 5.0 nm Pt/CMC (4.7±1.1 nm, Fig. S10) and 5.0 nm Pt/C (TEC10E50E-HT) were scrutinized. The 5.0 nm Pt/CMC still exhibited an enhanced SA relative to 5.0 nm Pt/C for the ORR (Fig. S11); whereas its enhancement factor is about 1.5 that is smaller than 2.1 for 2.1 nm Pt/CMC. This size-dependent enhancement factor can be rationalized with respect to that the small-sized metal NPs have the improved interfacial areas and an increased fraction of surface atoms that could be activated by the IGI. Notably, the metal clusters can present unusual nonequilibrium nature during reactions including large structural disorder, librational motion of the center of mass, and fluctuating bonding.[34, 66, 67] In this case, the dynamic flexible behaviour of metal clusters in order to respond the reacting conditions may have a much larger effect than the long-range IGI discussed here.[34] To describe the dynamic physical picture for flexible nanoclusters tethered to the support surface needs a close combination of theoretical simulations and operando characterization techniques.

Improved ORR durability by the IGI: The robust stability with high activity is indispensable for practical electrocatalysts. We examined the influence of IGI on stability by an accelerated durability test (ADT) as shown in Fig. 4c. After 30,000 loading cycles between 0.6 and 1.0 VRHE, 2.1 nm Pt/CMC lost only 21.3% MA and appears much more stable than 2.1 nm Pt/KB (54.2 % MA loss, Fig. 4d and Fig. S8). Moreover, the STEM images and element distributions of 2.1 nm Pt/CMC between the initial state (Fig. 4e) and after ADT (Fig. 4f) only show a small difference. These results demonstrate the improved stability for 2.1 nm Pt/CMC probably due to the cooperative effect between Pt NPs and Pt-CMC interfaces: (i) Pt-C interfaces are buried underneath and thus protected by Pt NPs; (ii) in turn, the IGI weakens Pt-O/OH binding and inhibit the electrochemical oxidation and dissolution of Pt NPs. This cooperation makes IGI more robust compared to other non-precious metals that induce lattice strain through an alloying effect but easily dissolve in a harsh ORR environment.

Interfacial Strain Field

Fig. 5

Attributes of the IGI: Here, to discuss the influence of IGI on electroactivity and stability of Pt NPs for the ORR, we introduce a model of interfacial strain filed (ISF) in Fig. 5a. The IGI induces an interfacial strain field for Pt atoms both at interfaces and adjacent to interfaces. The term "field" highlights the attribute of "long-range" impacting structures and the reactivity of Pt surface atoms more than a few atomic layers away from the interfaces.[27, 41, 43, 45] And the "anisotropy" attribute may be due to that the ISF varies at different crystallographic orientations (see the atomic-scale structural analysis). The "robust" attribute indicates the cooperative effect between Pt NPs and Pt-C interfaces making ISF more durable than do base metals (see the discussion in the stability section).

The Pt surface atoms affected by the IGI: According to strained states and geometric positions, Pt atoms in a cuboctahedron are classified into three types (see Fig. 5b). The Pt atoms at the center of interfaces are strongly strained but unexposed to ORR reactants. Secondly, the Pt atoms along interfacial perimeters are strongly strained and simultaneously available for ORR reactants. Thirdly, the Pt atoms adjacent to interfaces are strained by the long-range IGI and also accessible for ORR reactants. The enhanced ORR activity is, thus, contributed by the Pt surface atoms not only at interfacial perimeters but also adjacent to interfaces.

Possible factors affecting IGI: Herein, our observations suggest smaller metal NPs, for example, 2 versus 5 nm, has a larger enhancement factor presumably due to an increased fraction of surface atoms

activated by the IGI as compared with the larger NPs. Moreover, STEM energy dispersive spectroscopy (STEM-EDS) mapping shows that platinum is highly overlapped with oxygen (Fig. S12) because the oxygenated groups on carbon surface often act as anchoring sites for adsorption of the metal precursor and subsequent deposition of metal NPs. On the other hand, the metal NPs at stepped surfaces or edges of support are reported to strain or deform significantly.[49, 51] Here, the oxygenated groups on carbon surfaces may also promote IGI through strengthening interfacial affinity to Pt NPs to some extent. Theoretical calculations showed that the larger the concentration of oxygenated groups is and the closer they are to the Pt adatom, the stronger is the Pt binding energy to the carbon support.[32] However, there are huge complexities from both metals and supports in practical catalysts, the differences in lattice strains between NPs occur even in a catalyst (see the above HRTEM analysis). A comprehensive discussion is beyond the scope of current work and can be reached in a recent review.[28]

CONCLUSIONS

In summary, we provided evidence for the presence of interfacial geometric interactions (IGI) at metal-support interfaces on a basis of a combination of atomic-scale analysis of lattice strains, in-situ XAFS, and electrochemical measurements. The IGI shows long-range, anisotropic and robust attributes and impacts surface reactivity of the metals over several atomic layers far from the stressed metal-support interfaces. The surface atoms not only at interfacial perimeters but also vicinal interfaces are affected by the IGI and make their contribution to ORR activity enhancement. Current experimental findings and insights are expected to function for other metal-support systems.

EXPERIMENTAL SECTION

Chemicals. Carbon micro-coils (CMC) were provided by CMC General Research Institute in Gifu, Japan. Ethylene glycol, chloroplatinic acid hexahydrate, nitric acid, sodium hydroxide, and perchloric acid (TraceSELECT®) were all purchased from Sigma-Aldrich (research-grade) and used without further purification. Ultra-pure water (18 MΩ·cm) purified in a Millipore system was used in all experiments.

Chemical activation of CMC: CMC was chemically activated by 3 M nitric acid solution at 60°C for 48 h in which the surface graphene layer was partially oxidized to produce oxygenated species.

Preparation of 2.1 nm Pt/CMC, 2.1 nm Pt/KB and 4.7 nm Pt/CMC. Synthesis of the 2.1 nm Pt/CMC, the 2.1 nm Pt/KB and the 4.7 nm Pt/CMC were based on an ethylene glycol reduction method

as follows. Taking the 2.1 nm Pt/CMC as an example, 100 mg of CMC, 20 mL of ethylene glycol and 0.136 mL of 0.310 M chloroplatinic acid solution were added to a 150 ml pressure vessel. After 15-min stirring and 30-min ultra-sonication mixing, the pH of the mixing solution was adjusted to 10.0 using 0.1 M KOH solution. Then, the vessel was heated at 160 °C in an oil bath for 1 h. The obtained samples were filtered and rinsed by a mixture of ethanol and acetone (V/V=1/1), followed by dry at 60 °C under vacuum. The 2.1 nm Pt/KB was synthesized by a similar procedure except adding 0.410 mL of 0.310 M chloroplatinic acid solution. The 4.7 nm Pt/CMC was synthesized by a similar procedure without adjusting pH. A commercial Pt/C with an average size of around 2.0 nm (TEC10E20E, 19.0 wt% Tanaka Kikinzoku Kogyo (TKK)) and a Pt/C with an average size of 4-5 nm (TEC10E50E-HT, 50.9 wt.% TKK) were also used for comparison.

Electrochemical Measurements. All glassware for electrochemical measurements was treated by aqua regia and then by boiled water and washed by Millipore water thoroughly. A 0.1 M $HClO_4$ solution was prepared using perchloric Acid (TraceSELECT®, Sigma-Aldrich) and 18.2 MΩ·cm Millipore water. The electrocatalyst ink formulation is 1 mg electrocatalyst/0.5 mL Millipore water /0.4 mL isopropanol/0.005 ml 5 wt% Nafion®. The testing temperature is room temperature. Pt foil and RHE were used as counter and reference electrodes, respectively. Electrocatalyst thin-film working electrodes were prepared by a spin coating method on a 5 mm rotating disk electrode (RDE). The Pt loading on the RDE is about 12.2 $\mu g_{Pt} cm^{-2}$. The working electrodes were treated by an electrochemical activation process by repeated potential cycles (typically 50 cycles) from 0.02 to 1.2 V at a scan rate of 100 mV s^{-1} in N_2-saturated 0.1 M $HClO_4$ until a stable response was obtained. Cyclic voltammetry was measured at a scan rate of 50 mV s^{-1} in N_2-saturated 0.1 M $HClO_4$. Electrocatalytic performances for oxygen reduction reaction (ORR) were estimated by linear sweep voltammetry (LSV) from 0.0 to 1.05 V at a scan rate of 20 mV s^{-1} in O_2-saturated 0.1 M $HClO_4$ at 1600 rpm. The measurements were repeated three times and a maximum current among them at 0.9 V was used for calculations of mass activity (MS) and surface-specific activity (SA). The solution resistance R_{sol} was measured by the i-interrupter method and used for IR-compensation. Accelerated durability test (ADT) for loading cycles: ADTs were conducted by rectangular-wave 0.6 — 1.0 V potential cycles of 3 s at each of 0.6 and 1.0 V up to 30,000 cycles in O_2-saturated 0.1 M $HClO_4$.

TEM and STEM-EDS. TEM and STEM samples were prepared by dispersing electrocatalysts in ethanol by sonication, putting the dispersed electrocatalysts on carbon film deposited on Cu grids, and drying. We measured the interplanar spacing using a state-of-the-art microscope JEM-ARM200F that

allows observation of lattice with a spatial resolution of 0.7 Å (TEM mode). All imaging and analysis of interplanar spacing follow the same JEM-ARM200F apparatus and method between the two catalysts (2.1 nm Pt/CMC and 2.1 nm Pt/KB). Expectedly, there is the same statistical error produced by imaging and analysis of interplanar spacing of Pt NPs between the two catalysts. Part of TEM and STEM-EDS images were measured on a JEM-2100F equipped with an energy dispersive spectrometer (EDS) at 200 kV.

In-situ X-ray absorption fine structure (XAFS). All samples for in-situ XAFS experience the electrochemical pretreatment with that for the electrocatalytic measurements except particular statements. The electrocatalysts covered on rotating disk electrodes (RDE) was used as the working electrode for in-situ XAFS in N_2-saturated 0.1 M $HClO_4$ in a home-made electrochemical cell at 1600 rpm. The measurements of in-situ XAFS spectra at Pt L_3-edge were performed in a fluorescence mode by using a Si(111) double-crystal monochromator and an ion chamber (I_0: Ar 5% / N2 95%) for incident X-rays and a 21 Ge-elements detector for fluorescent X-rays at BL36XU station in SPring-8 similarly to the previous reports.[58, 60] X-ray absorption near-edge structure (XANES) spectra were normalized by Athena software. The XAFS spectra were treated with the data analysis program IFEFFIT (version 1.2.11c). Theoretical phase shifts and amplitude functions for Pt-Pt was calculated from FEFF 8.4. The extracted EXAFS oscillations were k^3-weighted and Fourier transformed to R-space. The curve fittings of k^3-weighted EXAFS data in R-space were carried out with Artemis.

XRD. X-ray diffraction patterns were measured on Rigaku RINT2000 with Cu Kα irradiation at 40 kV and 40 mA in the 2θ range of 10−90° at a step scan speed of 0.02^{o} s^{-1}.

XRF. X-ray fluorescence (XRF) analysis for bulk composition was conducted with Rigaku ZSX Primus2.

Electronic supplementary information (ESI) involving XRD, SEM, TEM/STEM/EDS, XAFS, and electrochemical data is available online.

Author contributions

X. Z., W. X., and ZW. C proposed and discussed the possible interfacial geometric interactions at metal-support interfaces. X. Z. synthesized electrocatalysts. X. Z., W. X., and ZW. C co-wrote the manuscript. X. Z., JB. Z, ML. X. JJ.G. and CP. L.conducted electrochemical experiments and discussed data. X. Z., T. K., Y. Y., T. S., K. H., and T. U. conducted in-situ RDE-XAFS tests. X. Z.and T. G. conducted high-

resolution TEM, STEM and EDX measurement. Y. Y. and X. Z. conducted SEM measurements. S. T. measured partial STEM images. F.T. provided constructive suggestions. All authors read and commented the manuscript.

Conflicts of interest

There are no conflicts to declare.

ACKNOWLEDGMENT

This work was supported by the New Energy and Industrial Technology Development Organization (NEDO) of Japan. This work was supported by the New Energy and Industrial Technology Development Organization (NEDO) of the Ministry of Economy, Trade, and Industry (METI), Japan. The financial support from the National Natural Science Foundation of China (21633008), the National Key R&D Program of China (Grant No. 2017YFB0102900) was appreciated. The authors appreciate the financial support from the Natural Sciences and Engineering Research Council of Canada (NSERC), the University of Waterloo, and the Waterloo Institute of Nanotechnology. The XAS measurements were performed with the approval of SPring-8 subject number 2018A7806, 2018B7800, 2019A7800 and 2019B7800. A part of HR-TEM measurements was conducted under the support of the NIMS microstructural characterization platform as a program of the "Nanotechnology Platform" of the Ministry of Education, Culture, Sports, Science, and Technology (MEXT), Japan. We thank the help of Y. Iwasawa for this project and his suggestion for utilizing CMC as support. We thank Dr. S. Motojima, President of CMC Advanced R&D Lab. Co. Ltd for providing CMC samples. F.T. acknowledges financial support from Chemical Sciences, Geosciences and Biosciences Division, Office of Basic Energy Sciences, Office of Science, U.S. Department of Energy, under Grant No. DE-SC0014561 and the NSF Career Award NSF-CHE-14162121.

REFERENCES

1. Z. W. Seh, J. Kibsgaard, C. F. Dickens, I. Chorkendorff, J. K. Nørskov and T. F. Jaramillo, *Science*, 2017, **355**.
2. M. K. Debe, *Nature*, 2012, **486**, 43-51.
3. H. A. Gasteiger, S. S. Kocha, B. Sompalli and F. T. Wagner, *Appl. Catal., B*, 2005, **56**, 9-35.
4. S. J. Tauster, S. C. Fung and R. L. Garten, *J. Am. Chem. Soc.*, 1978, **100**, 170-175.
5. Y. Liu and W. E. Mustain, *J. Am. Chem. Soc.*, 2013, **135**, 530-533.
6. Q. Jia, S. Ghoshal, J. Li, W. Liang, G. Meng, H. Che, S. Zhang, Z.-F. Ma and S. Mukerjee, *J. Am. Chem. Soc.*, 2017, **139**, 7893-7903.
7. J. A. Horsley, *J. Am. Chem. Soc.*, 1979, **101**, 2870-2874.

8. J. An, Y. Wang, J. Lu, J. Zhang, Z. Zhang, S. Xu, X. Liu, T. Zhang, M. Gocyla, M. Heggen, R. E. Dunin-Borkowski, P. Fornasiero and F. Wang, *J. Am. Chem. Soc.*, 2018, **140**, 4172-4181.
9. S. J. Tauster, *Acc. Chem. Res.* , 1987, **20**, 389-394.
10. J. C. Matsubu, S. Y. Zhang, L. DeRita, N. S. Marinkovic, J. G. G. Chen, G. W. Graham, X. Q. Pan and P. Christopher, *Nature Chem.*, 2017, **9**, 120-127.
11. X. Zhao, J. Zhu, L. Liang, J. Liao, C. Liu and W. Xing, *J. Mater. Chem.* , 2012, **22**, 19718-19725.
12. Z. P. Cano, D. Banham, S. Ye, A. Hintennach, J. Lu, M. Fowler and Z. Chen, *Nature Energy*, 2018, **3**, 279-289.
13. A. Rabis, P. Rodriguez and T. J. Schmidt, *ACS Catal.*, 2012, **2**, 864-890.
14. A. Chen and P. Holt-Hindle, *Chem. Rev.* , 2010, **110**, 3767-3804.
15. M. Shao, Q. Chang, J.-P. Dodelet and R. Chenitz, *Chem. Rev.* , 2016, **116**, 3594-3657.
16. I. E. L. Stephens, A. S. Bondarenko, U. Gronbjerg, J. Rossmeisl and I. Chorkendorff, *Energy Environ. Sci.* , 2012, **5**, 6744-6762.
17. M. Li, Z. Zhao, T. Cheng, A. Fortunelli, C.-Y. Chen, R. Yu, Q. Zhang, L. Gu, B. V. Merinov, Z. Lin, E. Zhu, T. Yu, Q. Jia, J. Guo, L. Zhang, W. A. Goddard, III, Y. Huang and X. Duan, *Science*, 2016, **354**, 1414-1419.
18. X. Huang, Z. Zhao, L. Cao, Y. Chen, E. Zhu, Z. Lin, M. Li, A. Yan, A. Zettl, Y. M. Wang, X. Duan, T. Mueller and Y. Huang, *Science*, 2015, **348**, 1230-1234.
19. C. Chen, Y. Kang, Z. Huo, Z. Zhu, W. Huang, H. L. Xin, J. D. Snyder, D. Li, J. A. Herron, M. Mavrikakis, M. Chi, K. L. More, Y. Li, N. M. Markovic, G. A. Somorjai, P. Yang and V. R. Stamenkovic, *Science*, 2014, **343**, 1339-1343.
20. X. Tian, X. Zhao, Y.-Q. Su, L. Wang, H. Wang, D. Dang, B. Chi, H. Liu, E. J. M. Hensen, X. W. Lou and B. Y. Xia, *Science*, 2019, **366**, 850-856.
21. J. K. Nørskov, J. Rossmeisl, A. Logadottir, L. Lindqvist, J. R. Kitchin, T. Bligaard and H. Jónsson, *J. Phys. Chem. B*, 2004, **108**, 17886-17892.
22. A. Kulkarni, S. Siahrostami, A. Patel and J. K. Nørskov, *Chem. Rev.* , 2018, **118** 2302–2312.
23. V. R. Stamenkovic, B. Fowler, B. S. Mun, G. F. Wang, P. N. Ross, C. A. Lucas and N. M. Markovic, *Science*, 2007, **315**, 493-497.
24. J. Greeley, I. E. L. Stephens, A. S. Bondarenko, T. P. Johansson, H. A. Hansen, T. F. Jaramillo, J. Rossmeisl, I. Chorkendorff and J. K. Norskov, *Nature Chem.*, 2009, **1**, 552-556.
25. V. Stamenkovic, B. S. Mun, K. J. J. Mayrhofer, P. N. Ross, N. M. Markovic, J. Rossmeisl, J. Greeley and J. K. Nørskov, *Angew. Chem. Int. Ed.*, 2006, **45**, 2897-2901.
26. V. Viswanathan, H. A. Hansen, J. Rossmeisl and J. K. Nørskov, *ACS Catal.*, 2012, **2**, 1654-1660.
27. P. Strasser, S. Koh, T. Anniyev, J. Greeley, K. More, C. Yu, Z. Liu, S. Kaya, D. Nordlund, H. Ogasawara, M. F. Toney and A. Nilsson, *Nature Chem.*, 2010, **2**, 454-460.
28. I. C. Gerber and P. Serp, *Chem. Rev.* , 2019.
29. M. Mahmoodinia, P.-O. Åstrand and D. Chen, *J. Phys. Chem. C*, 2016, **120**, 12452-12462.
30. M. Xu, S. Yao, D. Rao, Y. Niu, N. Liu, M. Peng, P. Zhai, Y. Man, L. Zheng, B. Wang, B. Zhang, D. Ma and M. Wei, *J. Am. Chem. Soc.*, 2018, **140**, 11241-11251.
31. T. Lunkenbein, J. Schumann, M. Behrens, R. Schlögl and M. G. Willinger, *Angew. Chem. Int. Ed.*, 2015, **54**, 4544-4548.
32. M. Mahmoodinia, P.-O. Åstrand and D. Chen, *J. Phys. Chem. C*, 2017, **121**, 20802-20812.
33. M. Mahmoodinia, M. Ebadi, P.-O. Åstrand, D. Chen, H.-Y. Cheng and Y.-A. Zhu, *PCCP* 2014, **16**, 18586-18595.
34. M. Mahmoodinia, T. T. Trinh, P.-O. Åstrand and K.-Q. Tran, *PCCP* 2017, **19**, 28596-28603.

35. L. Zhang, L. Y. Wang, C. M. B. Holt, T. Navessin, K. Malek, M. H. Eikerling and D. Mitlin, *J. Phys. Chem. C* 2010, **114**, 16463-16474.
36. L. Zhang, L. Y. Wang, C. M. B. Holt, B. Zahiri, Z. Li, K. Malek, T. Navessin, M. H. Eikerling and D. Mitlin, *Energy Environ. Sci.* , 2012, **5**, 6156-6172.
37. K. Sasaki, L. Zhang and R. R. Adzic, *PCCP* 2008, **10**, 159-167.
38. L. Zhang, L. Wang, C. M. B. Holt, T. Navessin, K. Malek, M. H. Eikerling and D. Mitlin, *J. Phys. Chem. C*, 2010, **114**, 16463-16474.
39. T. Ioannides and X. E. Verykios, *J. Catal.* , 1996, **161**, 560-569.
40. K. T. Chan, J. B. Neaton and M. L. Cohen, *Phys. Rev. B*, 2008, **77**, 235430.
41. H. Wang, S. Xu, C. Tsai, Y. Li, C. Liu, J. Zhao, Y. Liu, H. Yuan, F. Abild-Pedersen, F. B. Prinz, J. K. Nørskov and Y. Cui, *Science*, 2016, **354**, 1031-1036.
42. M. Mavrikakis, B. Hammer and J. K. Nørskov, *Phys. Rev. Lett.* , 1998, **81**, 2819-2822.
43. M. Luo and S. Guo, *Nature Reviews Materials*, 2017, **2**, 17059.
44. S. Schnur and A. Groß, *Phys. Rev. B*, 2010, **81**, 033402.
45. R. C. Cammarata, *Prog. Surf. Sci.* , 1994, **46**, 1-38.
46. E. D. Hermes, G. R. Jenness and J. R. Schmidt, *Molecular Simulation*, 2015, **41**, 123-133.
47. B. Liu, J. Liu, T. Li, Z. Zhao, X. Q. Gong, Y. Chen, A. J. Duan, G. Y. Jiang and Y. C. Wei, *J. Phys. Chem. C* 2015, **119**, 12923-12934.
48. E. Ochoa-Fernández, D. Chen, Z. Yu, B. Tøtdal, M. Rønning and A. Holmen, *Surf. Sci.* , 2004, **554**, L107-L112.
49. T. Daio, A. Staykov, L. M. Guo, J. F. Liu, M. Tanaka, S. M. Lyth and K. Sasaki, *Scientific Reports*, 2015, **5**.
50. A. Mishra, *Journal of material Science*, 2017.
51. W. Gao, A. S. Choi and J.-M. Zuo, *Surf. Sci.* , 2014, **625**, 16-22.
52. J. A. Enterkin, K. R. Poeppelmeier and L. D. Marks, *Nano Lett.* , 2011, **11**, 993-997.
53. J. Resasco, S. Dai, G. Graham, X. Pan and P. Christopher, *J. Phys. Chem. C*, 2018, **122**, 25143-25157.
54. M. Konsolakis, *Appl. Catal., B*, 2016, **198**, 49-66.
55. M. Klimenkov, S. Nepijko, H. Kuhlenbeck, M. Bäumer, R. Schlögl and H. J. Freund, *Surf. Sci.* , 1997, **391**, 27-36.
56. J. B. Wu, L. Qi, H. J. You, A. Gross, J. Li and H. Yang, *J. Am. Chem. Soc.*, 2012, **134**, 11880-11883.
57. W. J. Huang, R. Sun, J. Tao, L. D. Menard, R. G. Nuzzo and J. M. Zuo, *Nature Mater.*, 2008, **7**, 308.
58. X. Zhao, S. Takao, K. Higashi, T. Kaneko, G. Samjeskè, O. Sekizawa, T. Sakata, Y. Yoshida, T. Uruga and Y. Iwasawa, *ACS Catal.*, 2017, **7**, 4642-4654.
59. X. Zhao, T. Gunji, T. Kaneko, Y. Yoshida, S. Takao, K. Higashi, T. Uruga, W. He, J. Liu and Z. Zou, *J. Am. Chem. Soc.*, 2019, **141**, 8516-8526.
60. K. Nagasawa, S. Takao, S.-i. Nagamatsu, G. Samjeské, O. Sekizawa, T. Kaneko, K. Higashi, T. Yamamoto, T. Uruga and Y. Iwasawa, *J. Am. Chem. Soc.*, 2015, **137**, 12856-12864.
61. S. Mukerjee, S. Srinivasan, M. P. Soriaga and J. McBreen, *J. Electrochem. Soc.* , 1995, **142**, 1409-1422.
62. F. W. Lytle, P. S. P. Wei, R. B. Greegor, G. H. Via and J. H. Sinfelt, *The Journal of Chemical Physics*, 1979, **70**, 4849-4855.
63. Q. Jia, W. Liang, M. K. Bates, P. Mani, W. Lee and S. Mukerjee, *ACS Nano*, 2015, **9**, 387-400.
64. M. Teliska, W. E. O'Grady and D. E. Ramaker, *J. Phys. Chem. B* 2005, **109**, 8076-8084.
65. X. Zhao, T. Gunji, T. Kaneko, Y. Yoshida, S. Takao, K. Higashi, T. Uruga, W. He, J. Liu and Z. Zou, *J. Am. Chem. Soc.*, 2019.

66. F. Vila, J. J. Rehr, J. Kas, R. G. Nuzzo and A. I. Frenkel, *Phys. Rev. B*, 2008, **78**.
67. Y. He, J.-C. Liu, L. Luo, Y.-G. Wang, J. Zhu, Y. Du, J. Li, S. X. Mao and C. Wang, *Proceedings of the National Academy of Sciences*, 2018, **115**, 7700-7705.

Figures and captions

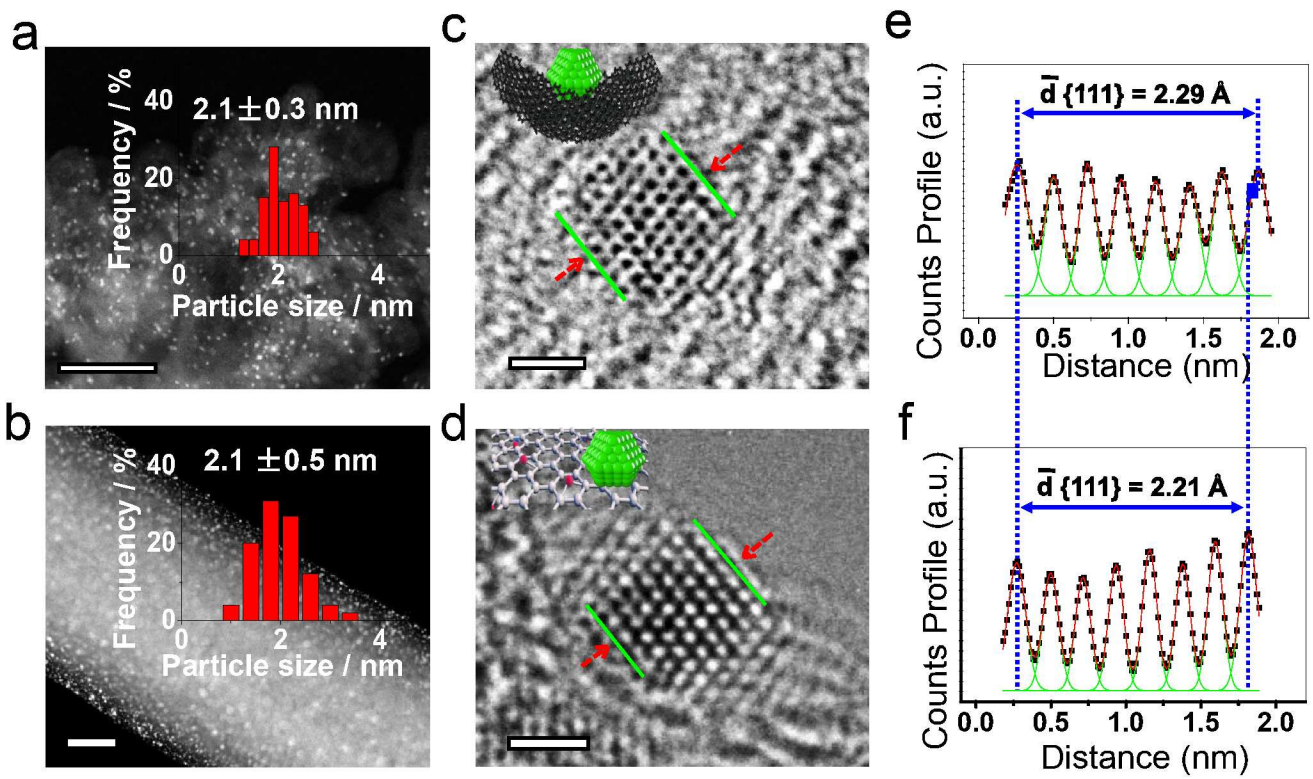

Fig. 1 Atomicscale evidence for the IGI. (a, b) High-angle annular dark-field scanning transmission electron microscopy (HAADF-STEM) images for the 2.1 nm Pt/KB (a) and the 2.1 nm Pt/CMC (b). (c, d) Atomically-resolved ATEM images for the KB-Particle-1 (c) and the CMC-Particle-1 (d). (e, f) Single-particle-based analysis of d{111} interplanar spacing for the KB-Particle-1(e) and the CMC-Particle-1(f). Scale bars in (a, b) and (c, d) are 50 and 1 nm, respectively. The insets in (a, b) and (c, d) are particle size distribution histograms and possible geometric configurations of Pt NPs on carbon, respectively.

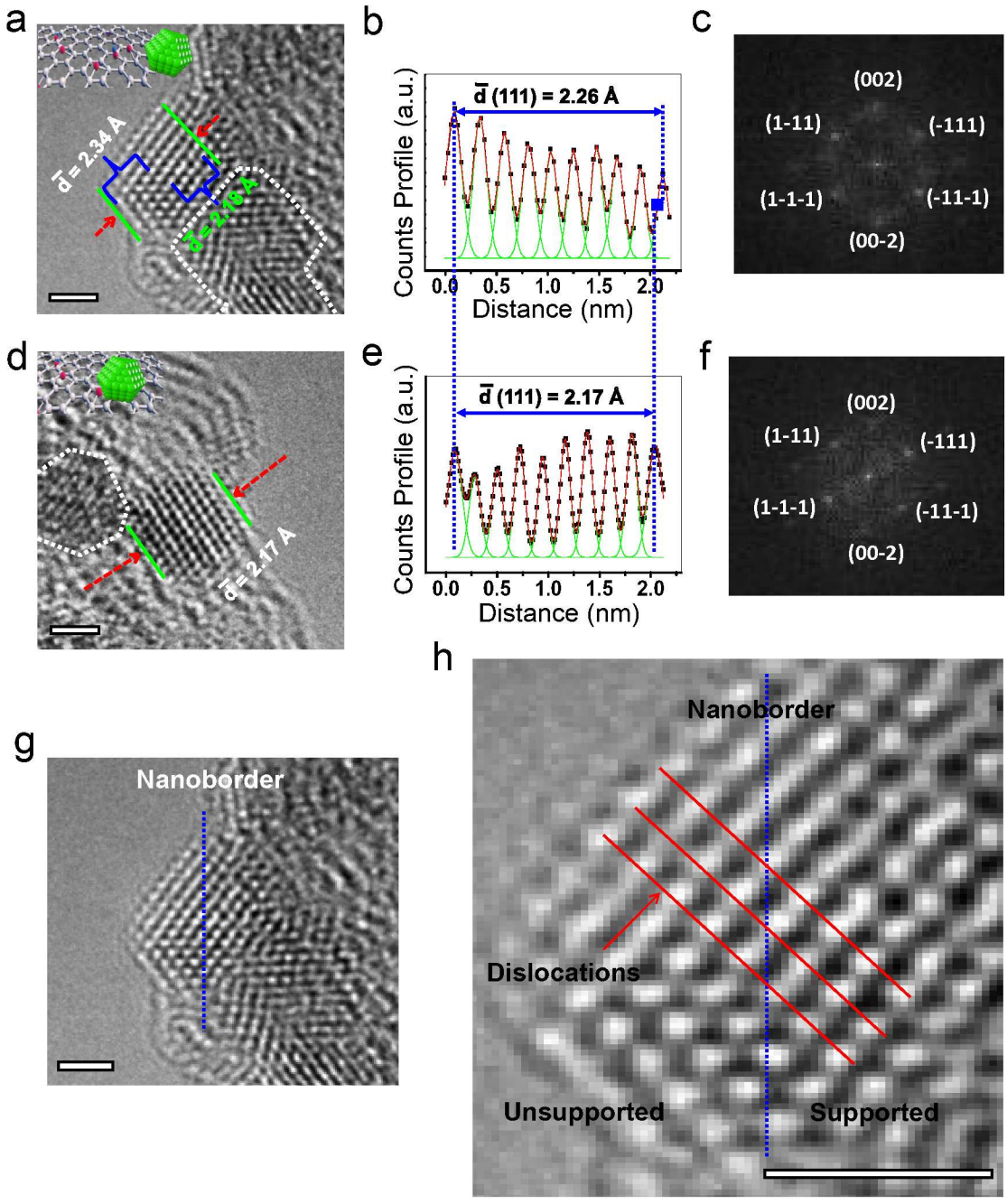

Fig. 2 Atomicscale evidence for the IGI. (a, d, g, h) atomically resolved ATEM images. (b, e) Analysis of d{111} interplanar spacing. (c, f) Fast Fourier Transform electron diffraction patterns. The Pt NPs in (a-c, g, h) and (d-f) are the CMC-particle-2 and the CMC-particle-3, respectively. The insets in (a, d) illustrate the discrepancy in interfacial areas between Pt NPs and CMC. Scale bars in (a, d, g, h) are 1 nm.

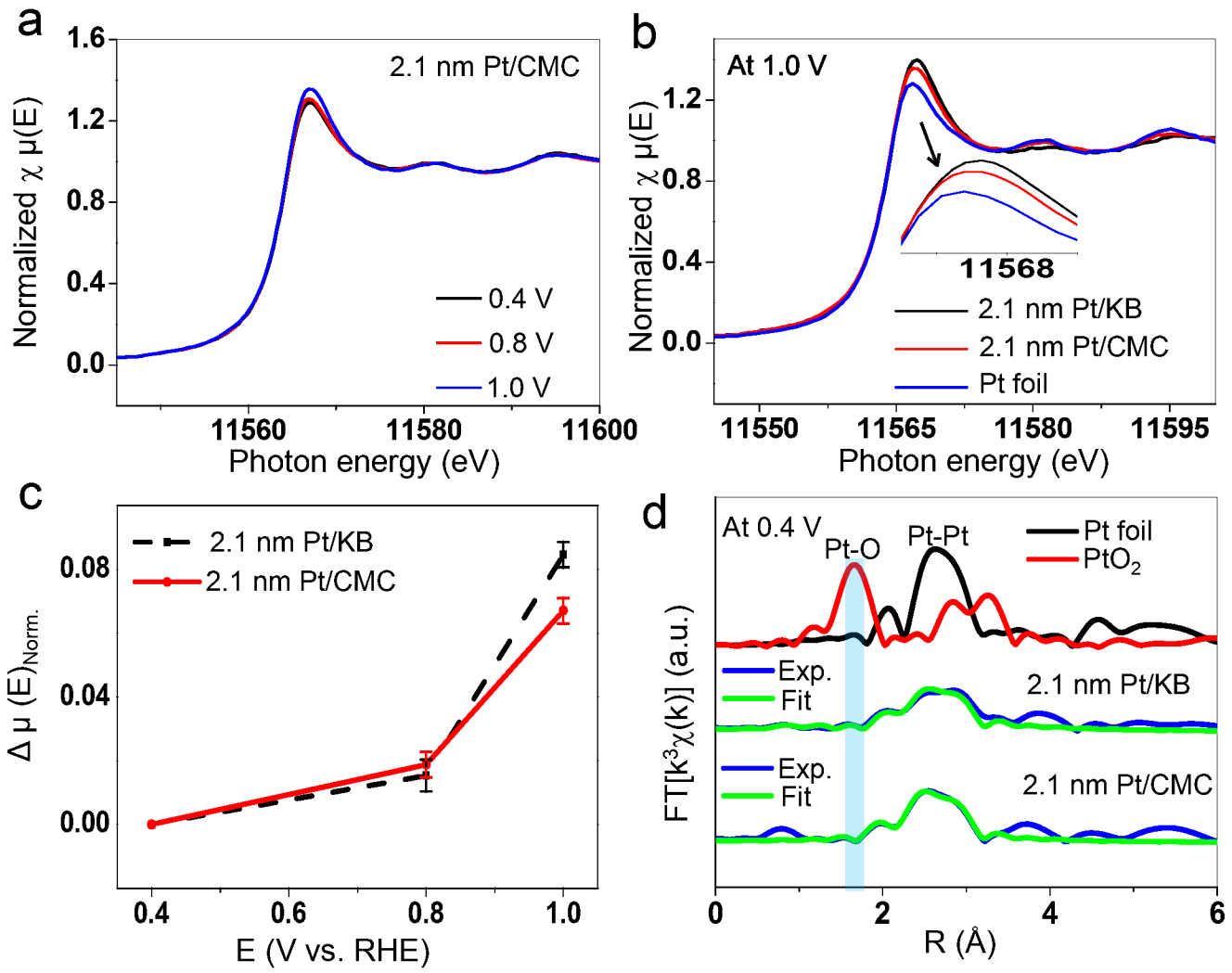

Fig. 3 In-situ spectroscopic evidence for the IGI. (a-b) In situ Pt L_3-edge XANES spectra of 2.1 nm Pt/CMC and 2.1 nm Pt/KB. (c) In-situ XANES analysis on Pt L_3-edge Δμ. ($\Delta\mu = \mu(E)_{norm}-\mu_{norm}(0.4\ V)$). (d) In-situ k^3-weighted Pt L_3-edge FT-EXAFS spectra at 0.4 V. A light blue rectangle region highlights that no Pt-C or Pt-O peaks can be assigned to 2.1 nm Pt/CMC and 2.1 nm Pt/KB.

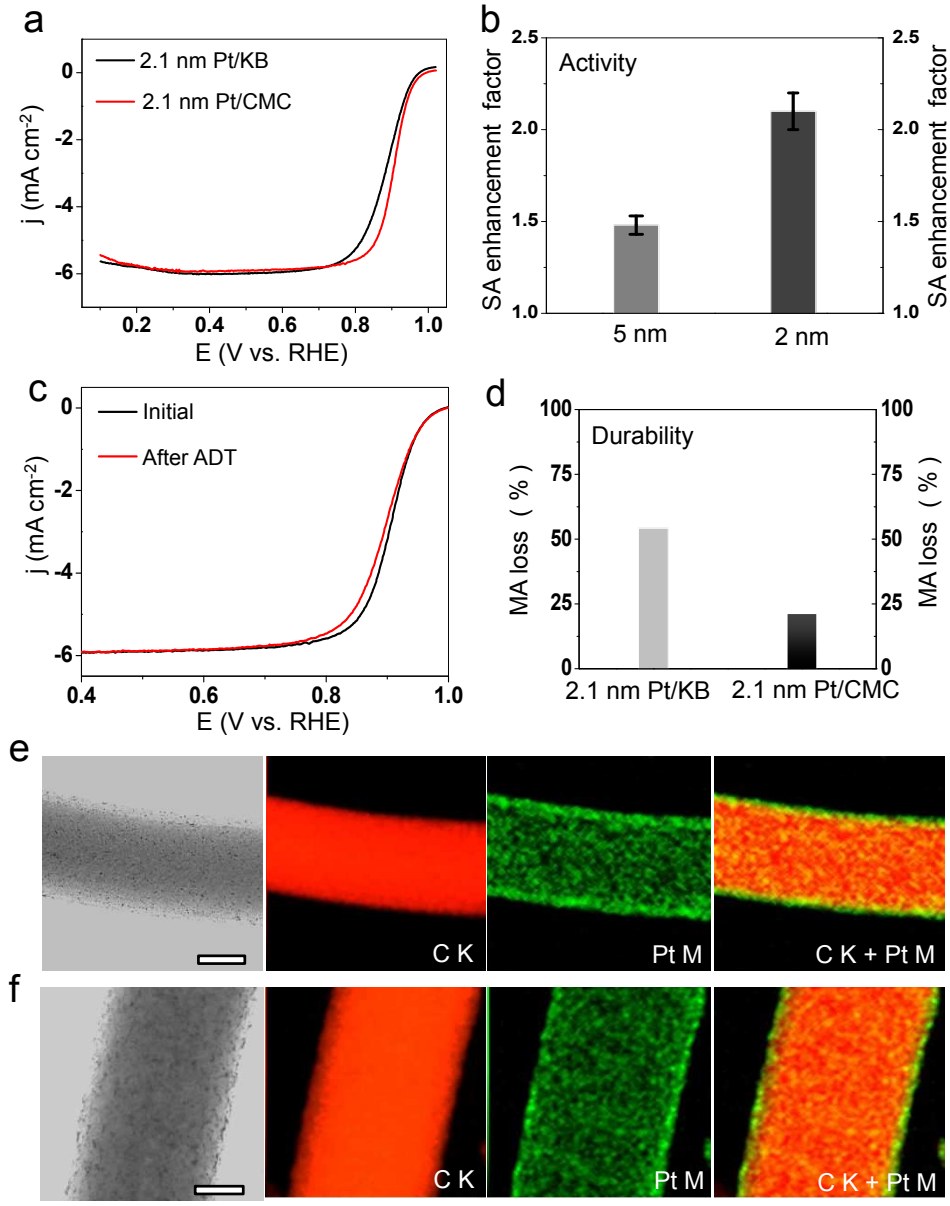

Fig. 4 Influences of the IGI on the activity and durability of Pt NPs for the ORR. (a) The ORR performances of catalysts evaluated by the anodic polarization in an O_2-saturated 0.1 M $HClO_4$ electrolyte at 1600 rpm with IR correction. (b) Size-dependent enhancement factors induced by the IGI on the basis of comparisons of the specific activity (SA) for 4.7 nm Pt/CMC vs. 5.0 nm Pt/C (TEC10E50E-HT) and 2.1 nm Pt/CMC vs. 2.1 nm Pt/KB. (c) The durability of 2.1 nm Pt/CMC after 30,000 potential cycles. (d) Comparisons of the durability between 2.1 nm Pt/KB and 2.1 nm Pt/CMC according to their mass activity (MA) loss after the ADT. (e, f) STEM-EDS images for 2.1 nm Pt/CMC before (e) and after (f) ADT. Scale bars in (e) and (f) are 200 and 100 nm, respectively.

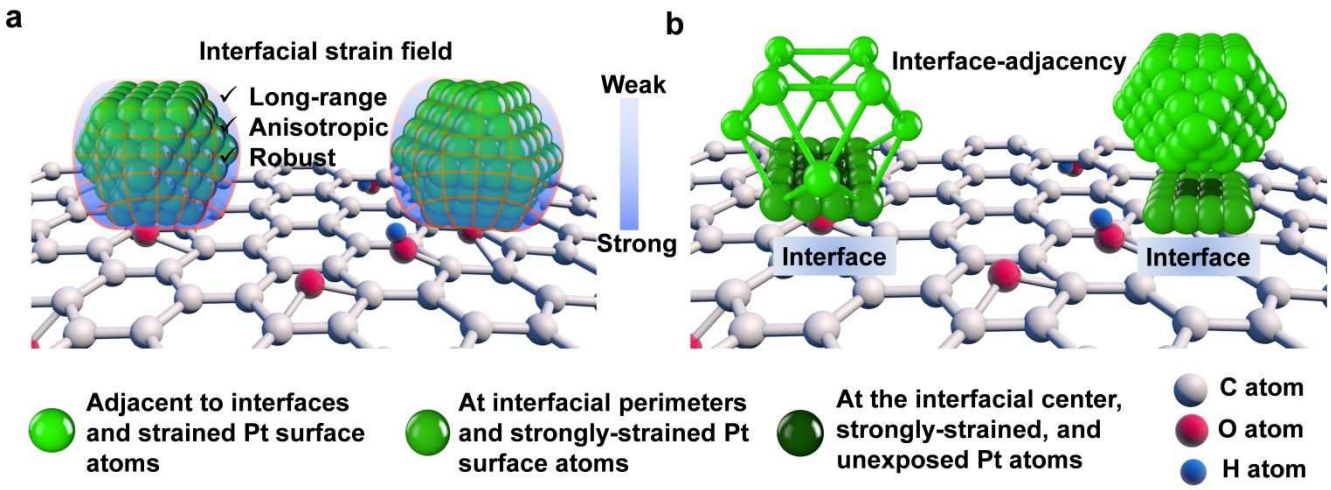

Fig. 5 Interfacial strain field model for the IGI. (a) Long-range, anisotropic and robust attributes for the IGI. Due to the atomic scale interphase or lattice mismatch at Pt-C interfaces (here Pt-CMC), the geometric strain initiates at Pt-C interfaces, evolves toward vicinal surface atoms and impacts their surface structure and catalytic behavior over several atomic layers far from the Pt-C interfaces. (b) Classification of surface sites in terms of their strained states and geometry locations. For clarity, a large part of Pt atoms was omitted in the particle at the left of Fig. 5b. The upper of the particle at the right of Fig. 5b was raised to highlight the interfacial/interface-on Pt atoms.

Graphical Abstract

We presented evidence for long-range interfacial geometric interactions at metal-support interfaces by a combination of atomic scale and in-situ characterizations.